Canted antiferromagnetic and optical properties of nanostructures of Mn_2O_3 prepared by hydrothermal synthesis*

Qurat-ul-ain Javed, Wang Feng-Ping†, M. Yasir Rafique, Arbab Mohammad toufiq, and M. Zubair Iqbal

Department of Physics, School of Mathematics and Physics, University of Science and Technology Beijing, Beijing 100083, *China*

(Received 26 June 2012; revised manuscript received 14 July 2012)

We have reported new magnetic and optical properties of Mn_2O_3 nanostructures. The nanostructures have been synthesized by the hydrothermal method combined with the adjustment of pH values in the reaction system. The particular characteristics of the nanostructures have been analyzed by employing X-Ray diffraction (XRD), scanning electron microscopy (SEM), energy dispersive X-ray (EDX) analysis, transmission electron microscopy (TEM), high resolution transmission electron microscopy (HRTEM), Raman spectroscopy (RS), UV–visible spectroscopy, and the vibrating sample magnetometer (VSM). Structural investigation manifests that the synthesized Mn_2O_3 nanostructures are orthorhombic crystal. Magnetic investigation indicates that the Mn_2O_3 nanostructures are antiferromagnetic and the antiferromagnetic transition temperature is at $T_N = 83$ K. Furthermore, the Mn_2O_3 nanostructures possess canted antiferromagnetic order below the Neel temperature due to spin frustration, resulting in hysteresis with large coercivity (1580 Oe) and remnant magnetization (1.52 emu/g). The UV–visible spectrophotometry was used to determine the transmittance behaviour of Mn_2O_3 nanostructures. A direct optical band gap of 1.2 eV was acquired by using the Davis–Mott model. The UV–visible spectrum indicates that the absorption is prominent in the visible region, and transparency is more than 80% in the UV region.

Keywords: Mn_2O_3 orthorhombic nanocrystals, UV transparency, canted antiferromagnetic property

PACS: 73.63.Bd, 78.40.–q, 75.10.–b, 75.75.–c **DOI:** 10.1088/1674-1056/21/11/117311

1. Introduction

Among the transition metals, manganese, because of its flexible variations in its local bonding configuration (2+, 3+, 4+) giving rise to a variety of manganese oxide as diverse as MnO, Mn_2O_3, Mn_3O_4, Mn_5O_8, and MnO_2, has attracted significant research efforts.[1] Manganese oxides are non-toxic, abundant, cost effective, and have a wide range of technical applications, including catalytic,[2] electrochemical,[3] magnetic,[4] optical,[5] and electrocatalytic biosensors.[6] In particular, Mn_2O_3 has attracted much interest as an anode material in the lithium ion battery. Moreover, Mn_2O_3 can also be used for preparing soft magnetic materials such as manganese zinc ferrite.[7]

Different types of nanostructures of α-Mn_2O_3, such as three-dimensional (3D) sponge-like porous hollow nanostructures,[8] spheres, dumbbell, and peanut-shaped microstructure, have already been reported. These microstructures mainly comprise wires/rods and particles have novel properties.[9,10]

The crystal structure of α-Mn_2O_3 is an undistorted cubic bixbyite above 302 K with Ia3 symmetry. Below this temperature, it has an orthorhombic crystal structure, which is distorted bixbyite as described by the space group Ia3.[11] The pure α-Mn_2O_3 bulk material has been found to be antiferromagnetic with a transition temperature of 80 K.[12−14] The second-order transition was also observed at $T = 40$ K in a sample prepared by solid-state reaction.[14] Tokeer *et al.* reported two transitions, one at $T =$ 80 K, and the other at 25 K in nanostructures of α-Mn_2O_3 prepared by thermal decomposition of manganese oxalate nano particles.[15] The neutron diffraction study on the magnetic structure of α-Mn_2O_3 by Regulski[11] showed the antiferromagnetic order from 80 to 100 K and a broad maximum of the magnetic susceptibility in this region. Canted anti-

*Project supported by the Fundamental Development Fund and Chancellor Scholarship Program, China (Grant No. YJ2010-014) and the Fundamental Research Funds for the Central Universities of China (Grant No. FRF-BR-09-007A).

†Corresponding author. E-mail: fpwang@ustb.edu.cn

© 2012 Chinese Physical Society and IOP Publishing Ltd

ferromagnetism plays an important role in the understanding of the physical properties of magnetic nanostructures and in the fabrications of new magnetic devices. Therefore, many studies on canted antiferromagnetic behaviour have been reported for different materials such as Fe_4Ni_2,[16] porous metal–organic framework,[17] and $M^{II}[N(CN)_2]_2$ (M=Co, Ni)H_2O.[18] Antiferromegnatic behaviour has been reported in undistorted cubic bixbyite α-Mn_2O_3, but few research ventures have been reported for the bixbyite orthorhombic phase of Mn_2O_3. In this paper, we have reported the synthesis of Mn_2O_3 nanostructures through the template-free hydrothermal route, and first reported the canted antiferromagnetic property and the UV transparency in the nanostructures of Mn_2O_3.

2. Experimental details

2.1. Sample preparation

Nanostructures of highly pure single-phase Mn_2O_3 were prepared by the hydrothermal method. In a typical procedure, pure Mn_3O_4 (3 gm) was added to 40-ml deionized water and stirred for 15 min. While stirring, a few drops of HNO_3 and ZrO_2 (0.003 gm) were added. The solution was magnetically stirred for another 15 min and a few more drops of HNO_3 were added. The pH value of the solution was 1.0. The solution was calcined in a stainless autoclave at 240 °C for 12 h. After the reaction was complete, the prepared product was filtered and dried at 70 °C for 6 h in an oven. The dried product was ground and mixed thoroughly using a pestle and mortar. ZrO_2 was used as a catalyst and filtered out.

2.2. Characterizations

Characterizations of the product were performed by X'Pert MPD (XRD) with Cu Kα radiation (λ = 0.154 nm), EDX (Hitachi S-3500 from 100 to 500 cps with 32-eV beam resolution), SEM (Hitachi S-3500), Raman spectroscopy (Horiba Jobin Yvon HR 800 Raman spectrometer with a 532-nm wavelength excitation), TEM (JEM-2010), HRTEM (JEM-2010), UV–visble spectroscopy (TU-1901), and VSM (QD Versa Lab).

3. Results and discussion

3.1. Morphology and structural properties

Figure 1 shows the XRD pattern of the as-synthesized product. All of the reflection in this pattern can be readily indexed to a bixbyite orthorhombic phase of Mn_2O_3 with the calculated lattice constant a = 0.941 nm, b = 0.942 nm, and c = 0.940 nm, respectively, which are in good agreement with the literature results (JCPS No 24-0508). From this pattern, it can be seen that the product has a high crystallinity. The plane (222) has the maximum intensity with the d-spacing of about 0.27 nm. The crystal size of the Mn_2O_3 nanostructures has been calculated according to the following Debye–Scherer formula:

$$Dc = K\lambda\beta^{-1}\cos\theta,$$

where $K = 0.9$ is the shape factor for tetragonal, λ is the X-ray wavelength (for CuKα), β is the full-width at half-maximum (FWHM) in radians, and θ is the position of the maximum of diffraction peak. By using the above equation, the average crystallite size was estimated to be about 39.17 nm.

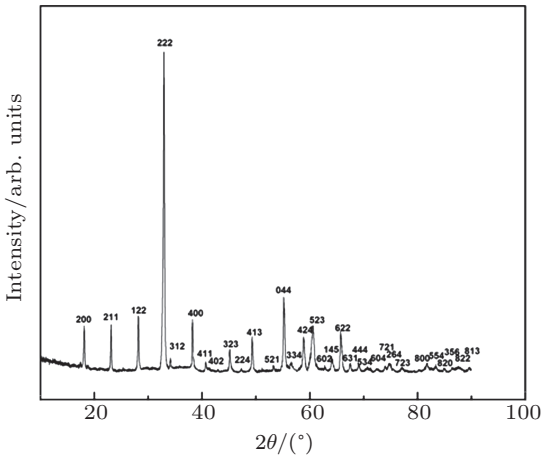


Fig. 1. X-ray diffraction pattern of Mn_2O_3.

Raman spectroscopy is a very functional technique used to investigate the microstructure of nano crystalline materials. Figure 2 shows the Raman spectrum of the nanostructures of Mn_2O_3, and five fundamental Raman modes at 651, 691, 367, 312, and 177 cm^{-1} are observed. The Raman spectrum of the orthorhombic Mn_2O_3 is similar to α-Mn_2O_3, which is coincident with the structural proximity of the two crystal phases.

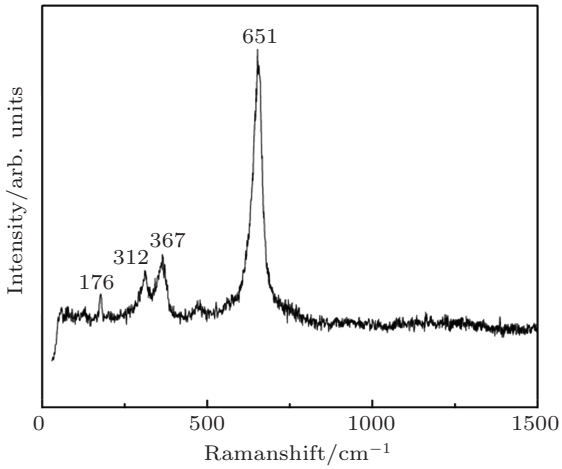


Fig. 2. Raman spectrum of the nanostructures of Mn_2O_3.

The morphology of the synthesized nanostructures was initially examined using SEM, as shown in Figs. 3(a) and 3(b). SEM results reveal a remarkable nanostructure of a Mn_2O_3 sample. Further examination reveals a more prominent nanostructure of the Mn_2O_3 sample, as shown in Fig. 3(b). From Fig. 3(b), it can be seen that the Mn_2O_3 exhibits layer-by-layer nanostructures, and the layers are interlinked with each other.

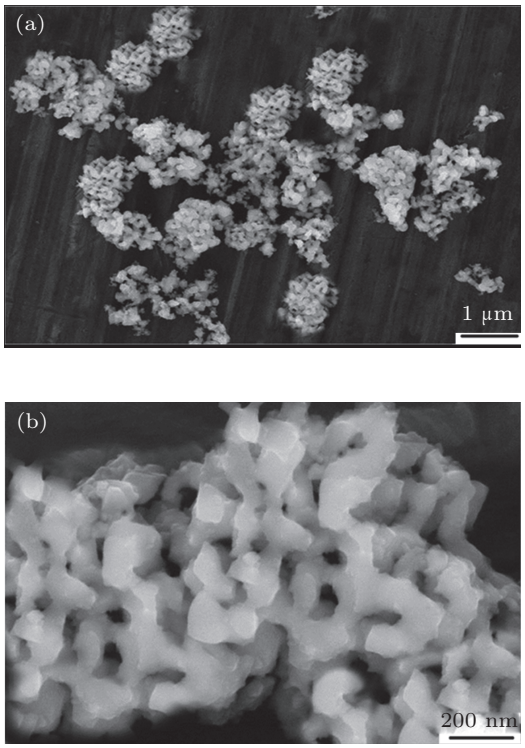


Fig. 3. SEM images of nanostructures of Mn_2O_3 at (a) low and (b) high magnification.

The elemental chemical composition of the nanostructures is investigated by EDX, as indicated in Fig. 4. The EDX spectrum shows the presence of Mn and O elements in the sample, while the signal of Cu peaks comes from the copper tape used for SEM measurements. The atomic percentage of Mn and O elements in the Mn_2O_3 sample is 13.44% and 86.56%, respectively. However, the actual stoichiometrical atomic percentage of Mn_2O_3 is 40% for Mn and 60% for O, which shows a deficiency of Mn in the sample.

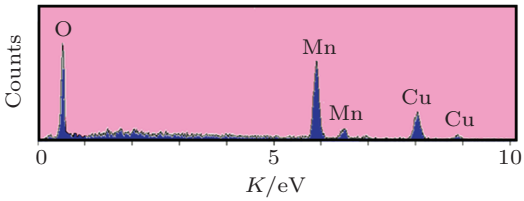


Fig. 4. (colour online) EDX analysis of the nanostructures of Mn_2O_3.

Mn deficiency may be due to the following reaction mechanism in the synthesis process of Mn_2O_3 nanostructures.

$$Mn_3O_4 \xrightarrow[ZrO_2]{} Mn_2O_3 + MnO, \quad (1)$$

$$MnO + 2HNO_3 \longrightarrow Mn(NO_3)_2 + H_2O. \quad (2)$$

In Eq. (1), the initial reagent Mn_3O_4 decomposes into Mn_2O_3 and MnO in the presence of strong acidic medium and high temperature. The resultant MnO reacts with HNO_3 in the solution, and $Mn(NO_3)_2$ and water are created and then washed out, which results in large Mn deficiency in the Mn_2O_3 nanostructures synthesized by the hydrothermal method.

Figure 5(a) presents a TEM image of a single nanostructure of Mn_2O_3 with a scale of 100 nm and an average width of about 40 nm for an individual nanostructure, which is comparable with the calculated crystallite size from the XRD by the Debye–Scherrer formula. Figure 5(b) shows that the nanostructure of Mn_2O_3 is structurally a uniform assembly in a single crystalline structure. The interlayer spacing was 0.27 nm, which is consistent with the corresponding 222 plane in XRD. The composition-determined growth of nanostructures into single-crystalline architectures is usually realized upon two factors: the controlled removal of appropriate additives (salt, ZrO_2, etc.) at interfaces, oriented attachment of nanostructures by re-organization of adjacent nanostructures, that ensures that they share an identical crystallographic orientation.[19]

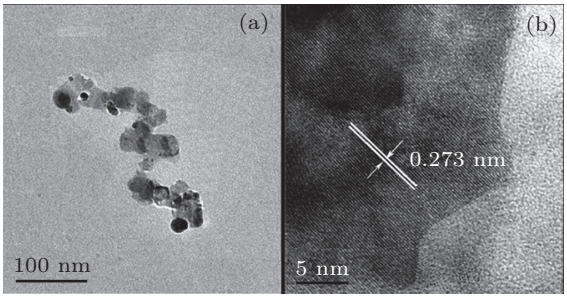


Fig. 5. (a) TEM image. (b) HRETM results of nanostructure of Mn_2O_3.

3.2. Magnetic properties

The magnetic properties of the Mn_2O_3 nanostructures are investigated. The field dependence of the magnetization M–H curve at room temperature exhibits the paramagnetic nature (Fig. 6(a)). To further investigate the magnetic behaviour of Mn_2O_3, we measured its magnetization as a function of the temperature. The M–T curve (Fig. 6(b)) shows that magnetization decreases linearly with temperature from 105 to 400 K, manifesting a paramagnetic nature. Moreover, the M–T curve shows a peak at the temperature of 83 K, which reveals an antiferromagnetic transition at $T_N = 83$ K. The temperature dependence of the reciprocal magnetic susceptibility χ^{-1} is shown by Fig. 6(c). It confirms the antiferromagnetic transition temperature at 83 K. The χ^{-1} obeys the Curie–Weiss law: $\chi = C/T - \Theta_a$, and χ^{-1} is proportional to temperature at high temperatures. By fitting the curve for the linear region and extrapolating, the extracted constants are $C = 0.0427$ emuK/g and $\Theta_a = -370$ K.

The slight difference of the Neel temperature between our result and the results previously reported may be attributed to either the nanostructure or the difference in the crystal structure, as the XRD result shows an orthorhombic crystalline structure rather than α-Mn_2O_3 in our sample. Ponpandian *et al.* observed that the Neel temperature of $Ni_{0.5}Zn_{0.5}Fe_2O_4$ increases due to the reduction of nano grain sizes.[20] We consider that spin frustration on the surface of nanostructure strengthens the magnetic interaction, resulting in the enhancement of Neel temperatures. In order to investigate the magnetic properties further, the field dependence of the magnetization M–H curve is measured at low temperature of $T = 65$ K, as shown in Fig. 6(d). Surprisingly, the M–H curve at $T = 65$ K shows large hysteresis, hence suggesting the ferromagnetic behaviour. Ferromagnetic parameters were calculated for remanence $M_R = 1.52$ emu/g and coercivity $H_C = 1580$ Oe at $T = 65$ K, respectively. Moreover, the magnetization will exceed 10 kOe. This peculiar phenomenon can be explained based on the ferromagnetism theory.

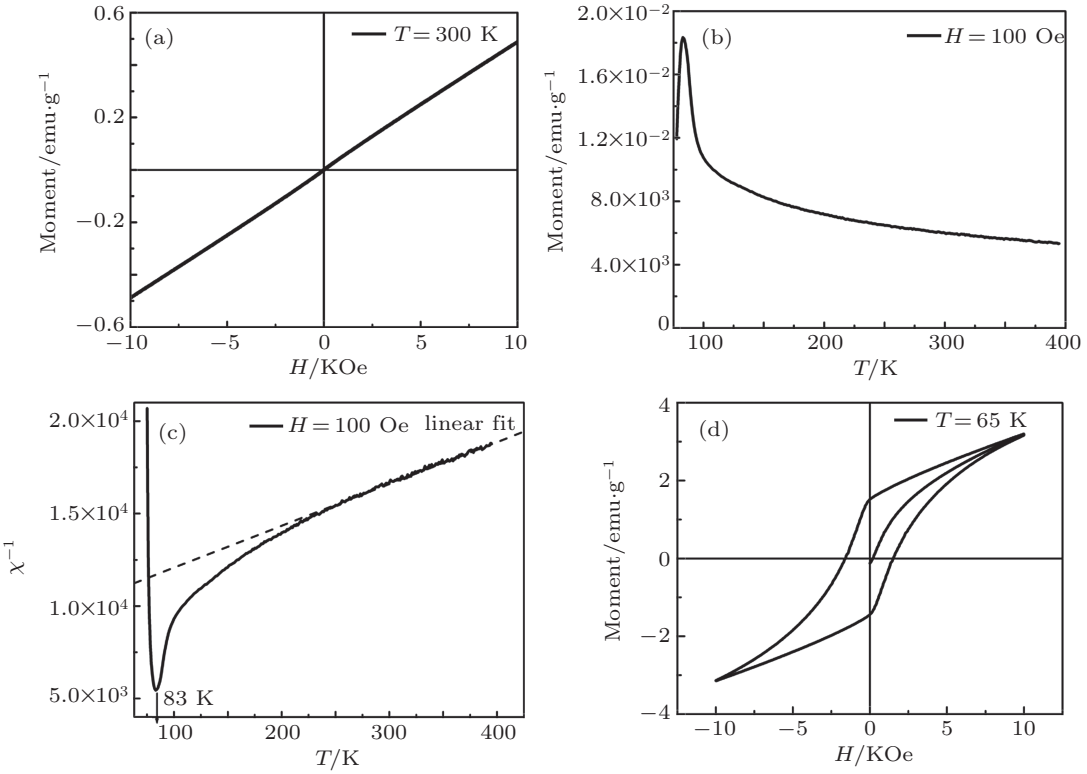


Fig. 6. (a) M–H curve at room temperature. (b) M–T curve under 100 Oe. (c) Temperature dependence of χ^{-1}. (d) M–H curve of nanostructure of Mn_2O_3 at 65 K.

The weak ferromagnetism and enhancement of magnetization below the Neel temperature in antiferromagnetic nano particles of $CoRh_2O_4$ is reported. The core shell model was used to explain the megnatic results of $CoRh_2O_4$. In this model, the core consists of antiferromagnetic spins, while the shell has a frustrated surface spin.[21] Similarly, the bulk NiO is an antiferromagnetic oxide. However, at nano scale, NiO was ferromagnetic with large magnetization of 100 emu/g, and with spin glass behaviours.[22] Makhlouf *et al.* showed that NiO nano particles also exhibit remarkable hysteresis at low temperatures, having remnant magnetization of 2 emu/g, coercivity of 4 kOe, and the hysteresis loop is open up to 55 kOe.[23] They suggested that uncompensated surface spin and exchange interaction between the AF core and uncompensated surface spin are responsible for this kind of peculiar behaviour. Therefore, in this context we can say that the ferromagnetic behaviour of the prepared Mn_2O_3 below the Neel temperature is due to nano-scale morphology effects.

Due to the nanostructures and Mn deficiency in the sample, the spin on the surface and edges of the chain may be uncompensated, resulting in canted antiferromagnetic rather than absolute AF on the surface. This point is illustrated in Fig. 7(a). In the antiferromagnetic (AF) structure where two sub-lattices have spin S_i and S_j ($S_i = -S_j$). The elimination of an isolated spin (e.g., S_j) will cause a series of magnetic frustration events in the vicinity of missing S_j spin. The first effect is the direct reduction of the exchange field H_{ex}, as the removal of S_j reduces the number of S_j nearest neighbours of spin S_i (z_{ij}^0) and numbers of S_j nearest neighbours of spin S_j (z_{jj}^0), hence reducing a component of an exchange field. The reduction of a component of the exchange field causes canted S_i spin in the vicinity of the S_j vacancy,[24] as shown by two red arrows enclosed in the circle in Fig. 7(a). Another effect is intersub-lattice spin canting, the dominant antiferromagnetic interaction between S_i and S_j intersub-lattice establishes the antiparallel spin alignments between them. The removal of spins from the j-th sub-lattice would have the indirect effect of causing the partial frustration of neighbouring spins of the i-th sub-lattice by spin canting, as indicated by the S_j (small) ring in Fig. 7(a). The third frustration effect occurs in the ring of S_i (large) nearest neighbours surrounding S_{i0} in the i-th sub-lattice. These three frustrations cause the construction of canted spin in the lattice which builds the hysteresis loop. The overall effect with these frustration effects is shown in Fig. 7(b), which shows that spin on the surface of the nanostructure becomes canted by surface vacancies of Mn and the core is antiferromagnetic, resulting in a net magnetic moment. Below the Neel temperature, when magnetic ordering occurs in the nanostructures of Mn_2O_3, the uncompensated surface spin, cause the canted antiferromagnetic structure resulting in the net magnetic moment and hysteresis. It may be supposed that the canted antiferromagnetic structure is the origin of ferromagnetic behaviour for nano-scale materials. Canted antiferromagnetic behaviour of Mn_2O_3 nanoparticles conduit towards different applications such as spin valves, reading head for magnetic storage media, and the memory element in magnetic random access memory.

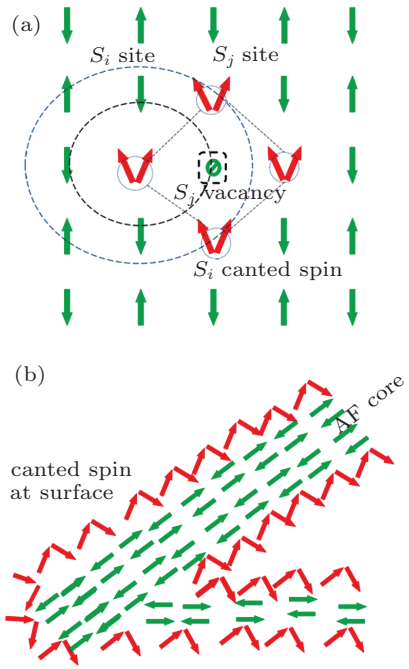


Fig. 7. (colour online) (a) Two-dimensional model of canted spin by vacancies. (b) Illustration of magnetic spin arrangement in nanostructures of Mn_2O_3.

3.3. Optical properties

Absorption spectrum of the Mn_2O_3 nanostructure in the range of 200–800 nm is shown in Fig. 8. It can be seen that the prepared sample of Mn_2O_3 absorbs photons strongly in the visible region and is highly transparent in the UV region. The absorption is more than 90% in the range of 440–725 nm, which forms an absorption band. As the wavelength decreases, the absorption decreases and transmission increases abruptly. The transmission spectrum is used to deter-

mine the absorption coefficient α as described below

$$\alpha = \frac{1}{d \ln(1/T)}, \tag{3}$$

where d is the path length and equal to 1 mm. The value of band gap and nature of optical interband transition is determined by Tauc and Davis–Mott models.

$$(\alpha h\nu)^n = A(h\nu - E_g), \tag{4}$$

where E_g is the band gap energy, A is constant, $n = 2$ for direct interband transition, and $n = 1/2$ for indirect transition. The straight line is only observed for $n = 2$, as shown in Fig. 8(b).[25] Therefore, the direct band gap is 1.2 eV which is obtained by extrapolating the linear part of the curve in Fig. 8(b) to the energy axis at $\alpha = 0$. The nanostructure shows prominent absorption in the visible region (400–800 nm). The absorption is more than 99% at the wavelength of 508 nm, and is 97% at the wavelength of 665 nm. The absorption of the nanostructures decreases with the increasing wavelength. On the other hand, transmission is more than 81% in the UV region (355–200 nm), as shown in Fig. 8(a). Additionally, the dips at 275 nm and 337 nm in the absorption spectrum may be due to the Mn deficiency in the compound. For wavelengths longer than 725 nm, absorption begins to decrease and transmission begins to increase. However, at the highest wavelength of 800 nm, the absorption is 62%, while the transmission is about 18%. Based on the above innovative results, we deduced that the nanostructures of Mn_2O_3 can be used for the applications where the absorption of visible light such as solar cells and photo-catalysts is required. It can also be used in applications where the transmission of UV light is required, such as UV filters and UV lasers.

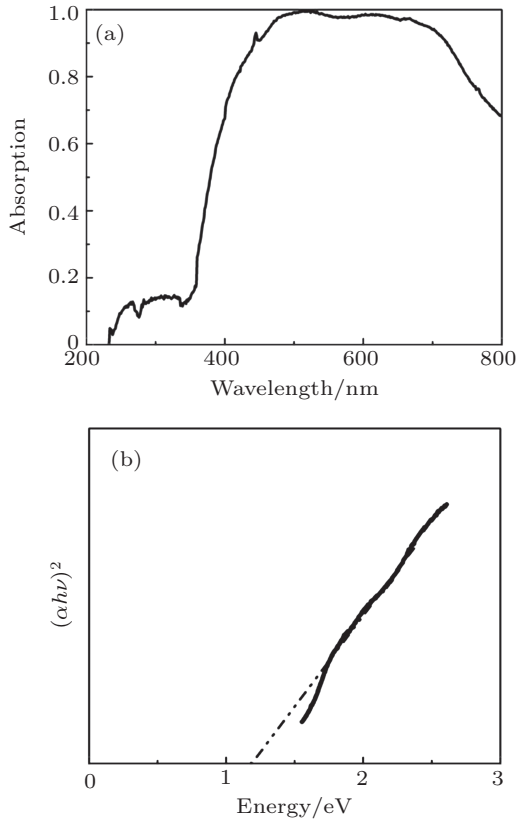


Fig. 8. UV–visible spectrum (a) Absorption. (b) Absorption coefficient versus energy.

4. Conclusions

Nanostructures with an average width of 40 nm were synthesized by a hydrothermal route at 240 °C. Structural analysis by XRD, Raman spectroscopy, TEM, and HRTEM confirms that the synthesized Mn_2O_3 is orthorhombic bixbyite. UV–visible spectra reveal that the absorption is more prominent in the visible region, while the transmission is more significant in the UV region. UV–visible spectra also demonstrate the direct band gap of 1.2 eV for Mn_2O_3 nanostructures. The nanostructures of Mn_2O_3 exhibited an antiferromagnetic transition at 83 K. Below the Neel temperature, large hysteresis is observed, which manifests the ferromagnetic behaviour. Based on the canted antiferromagnetism, the ferromagnetic behaviour is explained according to the spin frustration of nanostructures.

Acknowledgements

We appreciate the financial support of the University of Science and Technology, Beijing. We thank Mr. Huang Miao-Feng for his help in the measurement of magnetic properties, and Dr. Wang Ming-Wen for his help in the measurement of optical properties.

References

[1] Euna J, Changsoo K and Soonchil L 2011 *New J. Phys.* **13** 013018
[2] Yang Z, Zhang Y, Wang X, Qian Y, Wen X and Yang S 2006 *J. Solid State Chem.* **17** 679
[3] Thackeray M M 1997 *Prog. Solid State Chem.* **25** 1
[4] Lee H, Huh S H, Jeong J W, Choi Y J, Kim S H and Ri H C 2002 *J. Am. Chem. Soc.* **124** 12094
[5] Nasser A B M, DoWoo K, Ansari S G, Ahn K J, Kanjwal M A and Kim H K 2009 *Appl. Phys.* A **95** 769

[6] Jothiramalingam R and Wang M K 2101 *J. Porous. Mater.* **17** 677
[7] Chugai Electric Industrial Co. Ltd, Jpn. Kokai Tokyo Koho JP 02, 35915 [90, 35, 915], February 6 (1990)
[8] Yan D, Cheng S, Zhuo R F, Chen J T, Feng J J, Feng H T, Li H J, Wu Z G, Wang J and Yan P X 2009 *Nanotechnol.* **20** 105706
[9] Ashoka S, Chithaiah P, Tharamani C N and Chandrappaa G T 2010 *J. Exp. Nanosci.* **5** 285
[10] Yang Z, Zhang W, Wang Q, Song X and Qian Y 2006 *Chem. Phys. Lett.* **418** 46
[11] Regulski M, Przenioslo R, Sosnowska I, Howhlwein D and Schneider R 2004 *J. Alloys Compd.* **362** 236
[12] Geller S, Grant R W, Cape J A and Espinosa G P 1967 *J. Appl. Phys.* **38** 1457
[13] Grant R W, Geller S, Cape J A and Espinosa G P 1968 *Phys. Rev.* **175** 686
[14] Geller S and Espinosa G P 1970 *Phys. Rev.* B **1** 3763
[15] Ahmad T, Ramanujachary V K, Lofland E S and Ganguli K A 2004 *J. Mater. Chem.* **14** 3406
[16] Jinkwon K, Sujin H, Konstantin I P, Jesse M M and Joel S M 2005 *Inorg. Chem.* **44** 6983
[17] Xiang S, Wu X, Zhang J, Fu R, Hu S and Zhang X 2005 *J. Am. Chem. Soc.* **127** 16352
[18] Jamie L M, Carmen R K, Huang Q Z, Jeffrey W L, Goetz M B, Silvina P, Peter W S, Louise M L, Arnold L R, Arthur J E and Joel S M 1998 *Chem. Mater.* **10** 2552
[19] Zhang Z, Sun H, Shao X, Li D, Yu H and Han M 2005 *Adv. Mater.* **17** 42
[20] Ponpandian N, Narayanasamy, Chinnasamy C N and Sivakuma N 2005 *Appl. Phys. Lett.* **86** 192510
[21] Bhowmik R N 2004 *Phys. Rev.* B **169** 054430
[22] Yi J B, Ding J, Feng Y P, Peng G W, Chow G M, Kawazoe Y, Liu B H, Yin J H and Thongmee S 2007 *Phys. Rev.* B **76** 224402
[23] Makhlouf S A, Parker F T, Speda F E and Berkowitz A E 1997 *J. Appl. Phys.* **81** 5561
[24] Dionne F G 2009 *Magnetic Oxides* **161**
[25] He X, Wu J, Zhao L, Meng J, Gao X and Li X 2008 *Solid State Commun.* **147** 90
[26] Xiang X, Cheng X F, He S B, Yuan X D, Zheng W G, Li Z J, Liu C M, Zhou W L and Zhu X T 2011 *Chin. Phys.* B **20** 127801